International Journal of Nanomedicine

Dovepress
open access to scientific and medical research

Open Access Full Text Article

ORIGINAL RESEARCH

Identification of the Vulnerability of Atherosclerotic Plaques by a Photoacoustic/Ultrasonic Dual-Modal cRGD Nanomolecular Probe

Caigui Yu[1–3,*], Lu Zhong[1–3,*], Yanxiang Zhou[1–3,*], Nan Jiang[1–3], Jinling Chen[1–3], Sheng Cao[1–3]

[1]Department of Ultrasound Imaging, Renmin Hospital of Wuhan University, Wuhan, 430060, People's Republic of China; [2]Hubei Key Laboratory of Cardiology, Wuhan, 430060, People's Republic of China; [3]Cardiovascular Research Institute, Wuhan University, Wuhan, 430060, People's Republic of China

*These authors contributed equally to this work

Correspondence: Jinling Chen; Sheng Cao, Department of Ultrasound Imaging, Renmin Hospital of Wuhan University, 238# Jiefang Road, Wuhan, 430060, People's Republic of China, Email jenny2774@163.com; caosheng209@126.com

Objective: To explore the feasibility of using cRGD-GNR-PFP-NPs to assess plaque vulnerability in an atherosclerotic plaque mouse model by dual-modal photoacoustic/ultrasonic imaging.

Methods: A nanomolecular probe containing gold nanorods (GNRs) and perfluoropentane (PFP) coated with the cyclic Arg-Gly-Asp (cRGD) peptide were prepared by double emulsion solvent evaporation and carbodiimide methods. The morphology, particle size, potential, cRGD conjugation and absorption features of the nanomolecular probe were characterized, along with its in vitro phase transformation and photoacoustic/ultrasonic dual-modal imaging properties. In vivo fluorescence imaging was used to determine the distribution of cRGD-GNR-PFP-NPs in vivo in apolipoprotein E-deficient ($ApoE^{-/-}$) atherosclerotic plaque model mice, the optimal imaging time was determined, and photoacoustic/ultrasonic dual-modal molecular imaging of integrin αvβ3 expressed in atherosclerotic plaques was performed. Pathological assessments verified the imaging results in terms of integrin αvβ3 expression and plaque vulnerability.

Results: cRGD-GNR-PFP-NPs were spherical with an appropriate particle size (average of approximately 258.03±6.75 nm), a uniform dispersion, and a potential of approximately −9.36±0.53 mV. The probe had a characteristic absorption peak at 780~790 nm, and the surface conjugation of the cRGD peptide reached 92.79%. cRGD-GNR-PFP-NPs were very stable in the non-excited state but very easily underwent phase transformation under low-intensity focused ultrasound (LIFU) and had excellent photoacoustic/ultrasonic dual-modal imaging capability. Mice fed a high-fat diet for 20 weeks had obvious hyperlipidemia with larger, more vulnerable plaques. These plaques could be specifically targeted by cRGD-GNR-PFP-NPs as determined by in vivo fluorescence imaging, and the enrichment of nanomolecular probe increased with the increasing of plaque vulnerability; the photoacoustic/ultrasound signals of the plaques in the high-fat group were stronger. The pathological assessments were in good agreement with the cRGD-GNR-PFP-NPs plaque accumulation, integrin αvβ3 expression and plaque vulnerability results.

Conclusion: A phase variant photoacoustic/ultrasonic dual-modal cRGD nanomolecular probe was successfully prepared and can be used to identify plaque vulnerability safely and effectively.

Keywords: atherosclerosis, vulnerability, photoacoustic, ultrasound, low-intensity focused ultrasound

Introduction

Currently, the incidence and mortality rates of cardiovascular diseases remain high, which has caused great social and economic losses.[1] Studies have shown that secondary thrombosis after atherosclerotic plaque rupture or erosion is one of the most important pathogeneses of myocardial infarction, ischemic stroke and other cardio-cerebrovascular incidents.[2,3] These "criminal plaques" that easily rupture or erode and cause secondary thrombosis are called vulnerable plaques.[4] The progression of an atherosclerotic plaque is silent, and timely monitoring and effective evaluation of plaque vulnerability have become important in the prevention and treatment of acute cardio-cerebrovascular events.

Received: 30 April 2024
Accepted: 3 September 2024
Published: 11 September 2024

With the rapid development of imaging technology, the detection rate of atherosclerotic plaques has been greatly improved, but assessing the vulnerability of plaques is still a serious challenge. An increasing number of technologies, including intravascular ultrasound (IVUS) and optical coherence tomography (OCT), are advancing in the assessment of atherosclerotic plaque vulnerability.[5] However, achieving accurate and dynamic monitoring is difficult. Photoacoustic (PA) imaging has the advantages of strong penetration depth and high contrast and resolution, and uses nonionizing radiation for noninvasive imaging.[6] As a classical noninvasive imaging method, ultrasound can dynamically allow visualization of the tissue morphology, and multidimensional anatomical structure and component information can be acquired when ultrasound is combined with PA imaging.[7] Moreover, after the addition of highly specific and multi-functional molecular probes, more accurate molecular functional information can be obtained, which can be used to assess plaque vulnerability.

Gold nanorods (GNRs) exhibit strong light absorption characteristics and excellent light scattering properties in the near-infrared region (NIR) by virtue of the plasmon resonance effect generated on their surface. GNRs have become the most widely used PA imaging contrast agents due to their advantages, such as good biocompatibility and low cytotoxicity.[8] Therefore, GNRs can be used as a core component of photoacoustic/ultrasonic dual-modal nanomolecular probes. The nanomolecular probes containing phase change material can undergo liquid-gas phase transition under low-intensity focused ultrasound (LIFU) irradiation, which then causes the expansion of the nanomolecular probes to enhance the effect of ultrasonic imaging. As a phase change material with a relatively low boiling temperature (only 29 °C), perfluoropentane (PFP) was more likely to undergo liquid-gas phase transition under LIFU irradiation and was widely used in nanomolecular probes.[9] Nanomolecular probes need not only excellent multimodal imaging capabilities but also specific molecular recognition elements to bind specifically to atherosclerotic plaque vulnerability-related biomarkers. The glycoprotein receptor integrin αvβ3 is highly expressed in neovascular endothelial cells and the CD68-positive macrophages surrounding the plaque necrotic core and can be used as a substitute parameter for plaque vulnerability.[10] The arginine-glycine-aspartate (Arg-Gly-Asp, RGD) peptide sequence can bind specifically to integrin αvβ3 and thus be used as a target recognition group for atherosclerotic plaque vulnerability. The RGD peptide could be coupled on a PET-CT molecular probe to trace the expression of αvβ3 in atherosclerotic plaques, and the results were consistent with the pathological assessment data.[11] The combination of photoacoustic imaging, αvβ3 and GNRs offered sensitive and specific discrimination and quantification of angiogenesis in vivo, which may be clinically applicable to a variety of highly prevalent diseases, including cardiovascular disease.[12] RGD targeted nanoprobe had been performed during the molecular imaging of angiogenesis in atherosclerotic plaques by photoacoustic/ultrasound.[13] The RGD modified nano-molecular could be used as a photoacoustic contrast agent for selectively lightening early thrombus with high photo-acoustic intensity, good stability in light and serum, and sufficient blood-circulating half-life in mice.[14] Thus, the use of RGD-modified molecular probes is expected to mediate the photoacoustic/ultrasonic assessment of plaque vulnerability.

Therefore, the intent of this study is to construct a photoacoustic/ultrasonic dual-modal RGD nanomolecular probe that can be used as a photoacoustic/ultrasonic imaging agent to enhance the ultrasound imaging effect while specifically targeting atherosclerotic plaques for vulnerability assessment.

Methods

Preparation of cRGD-GNR-PFP-NPs

12.5 mg carboxy-terminated poly (lactic-co-glycolic acid) (PLGA-COOH, Jinan Daigang Biomaterial, China) was dissolved in 1 mL of dichloromethane in an ice bath. Then, 150 μL of a 0.1 mg/mL solution of GNRs (Nanoseedz, Hong Kong, China) was placed in 100 μL of perfluoropentane in an ice bath and treated with vibration for 1 min (pulse 5/5; amp 100%; 120 W) to obtain a gray initial emulsion. The initial emulsion was added to the PLGA-COOH solution, and the mixed liquid was treated with vibration in an ice bath for 2 min to obtain a gray-white compound emulsion. Then, 1.25 mL of 4% poly (vinyl alcohol) solution was added, and the mixture was fully homogenized with a high-speed dispersion homogenizer for 2 min. Next, 2.5 mL of 2% isopropyl alcohol was added, and the mixture was magnetically stirred for 4 h to fully volatilize the dichloromethane. The suspension that was obtained was centrifuged at 1500 rpm and 4°C. The obtained precipitate was centrifuged at 12,000 rpm and then suspended in ultrapure water. This process was

repeated three times, yielding the precipitated GNRs and perfluoropentane (PFP, J&K Scientific, Beijing, China) nanoprobe GNR-PFP-NPs, which were stored under cold conditions.

A 0.1 M 2-Morpholinoethanesulfonic acid monohydrate (MES, Aladdin Biotech, China) solution was prepared with ultrapure water, and NaOH was added to adjust the pH to 5.7. GNR-PFP-NPs were resuspended in the pH-adjusted MES to generate a GNR solution, while the coupling activators 1-ethyl-3-(3-dimethylaminopropyl) carbodiimide (EDC, Aladdin Biotech, China) and N-hydroxysuccinimide (NHS, Sigma-Aldrich, America) were fully dissolved in MES to generate an activator solution. At a molar ratio of PLGA-COOH:EDC:NHS=1:2:1, EDC and NHS were successively added to the GNR-PFP-NPs solution, and the reaction was carried out at 4°C for 3 h. The excess EDC and NHS were removed by performing multiple centrifugation rinse steps, leaving the activated GNR-PFP-NPs. NaOH was added to the solution to adjust the pH to 8.0, the activated GNR-PFP-NPs were resuspended in the MES solution, and cyclic Arg-Gly-Asp (cRGD, Shending Biotech, Shanghai, China) was dissolved in MES for use. After the quantity of carboxyl groups in PLGA-COOH was determined, an equal molar amount of cRGD was added to the solution, the reaction was carried out at low temperature for 12 h. Finally, the cRGD-modified nanoprobe (cRGD-GNR-PFP-NPs) was obtained after resuspension and washing with PBS (Servicebio, China). The prepared molecular probes GNR-PFP-NPs and cRGD-GNR-PFP-NPs were diluted with PBS, and their particle size and potential were measured with a laser particle size potentiometer (Nano ZSP, Malvern, Britain). The surface morphology of molecular probe was observed by scanning electron microscope (SEM, ZEISS, GeminiSEM 500, Germany).

The Conjugation Detection of the cRGD Peptide to GNR-PFP-NPs

The red fluorescent dye 1,1′-dioctadecyl-3,3,3′,3′-tetramethylindocarbocyanine perchlorate (DiI, Yuanye Biotech, Shanghai, China) was dissolved in dichloromethane during the preparation of the GNR-PFP-NPs. Additionally, cRGD was labeled by fluorescein isothiocyanate (FITC) to generate FITC-cRGD with green fluoresce. The DiI and FITC dual-channel molecular probes were observed by laser confocal microscopy. Three hundred microliters of conjugated FITC-cRGD-GNR-PFP-NPs and DiI-GNR-PFP-NPs were used for flow cytometry fluorescence detection to quantify the conjugation rates of FITC-cRGD and GNR-PFP-NPs.

cRGD-GNR-PFP-NPs Infrared and Ultraviolet Absorption Spectrum Analysis

cRGD, cRGD-GNR-PFP-NPs and GNR-PFP-NPs were freeze-dried, and their freeze-dried powders were mixed and ground with dried potassium bromide powder. After being fully ground, each probe sample was added to the grinding tool and pressed into a thin slice for infrared absorption spectrum analysis. Moreover, cRGD-GNR-PFP-NPs, cRGD-PFP-NPs and GNR solutions were prepared at appropriate concentrations and added to a colorimetric dish for ultraviolet absorption spectral analysis in the wavelength range of 350~900 nm.

The Phase Transformation and Ultrasonic Imaging of cRGD-GNR-PFP-NPs by LIFU Irritation

The agarose gel model was prepared firstly. 3g agarose powder was added into 100 mL ultra-pure water, which was heated and dissolved in a microwave oven. After stirring well, the gel was introduced into the mold, and 1.5 mL centrifuge tube was inserted into the gel, which was fixed until the gel cooled and solidified, and then the centrifuge tube was removed to obtain the gel model with holes. One milliliter of a 2.0 mg/mL cRGD-GNR-PFP-NPs solution was placed in the agarose gel well and irradiated by LIFU (ultrasonic frequency, 2000 kHz; ultrasonic intensity, 1.5 W/cm^2; modulation frequency, 3000 Hz; and duty cycle, 30%). Invert optical microscope (IX51, Olympus, Tokyo, Japan), brightness mode (B-mode) ultrasound and contrast-enhanced ultrasonography (CEUS) were performed after the nanoprobes were irradiated for 1 min, 2 min, 3 min, 4 min and 5 min.

cRGD-GNR-PFP-NPs Photoacoustic Imaging in vitro

The photoacoustic imager (Vevo LAZR, Fujifilm Visual Sonics, Canada) was equipped with a pulsed tunable laser for photoacoustic imaging in the NIR (the wavelength range of 680–970 nm) and ultrasonic probe MX550D (26–52 MHz,

center frequency 40 MHz), which was used to stimulate the cRGD-GNR-PFP-NPs solution in the agarose in various Eppendorf tubes and fixed into the water tank for photoacoustic imaging, and the photoacoustic signal intensity-wavelength curve of the nanoprobe was constructed to determine the optimal excitation wavelength. Then, the cRGD-GNR-PFP-NPs were diluted with PBS to different concentrations (0, 0.5 mg/mL, 1.0 mg/mL, 2.0 mg/mL, 4.0 mg/mL and 8.0 mg/mL). The photoacoustic signals of them were collected at the optimum wavelength.

In vitro Cell Survival Assay

The survival rates of human umbilical vein endothelial cells (HUVECs, Center for Type Culture Collection, Wuhan, China) cultured with cRGD-GNR-PFP-NPs for 12 h and 24 h were detected by cell counting kit-8 assays (Dojindo, Japan). Culture medium containing cRGD-GNR-PFP-NPs (0, 0.5 mg/mL, 1.0 mg/mL, 2.0 mg/mL, 4.0 mg/mL and 8.0 mg/mL) was added to the well plate, with 5 duplicate wells for each group and another 5 wells used as blanks. The plate was incubated for 12 h or 24 h, after which the absorbance was measured at 450 nm using an enzyme-labeled instrument. The cell survival rate was calculated as follows: Cell survival rate (%) = $(A_{nanoprobe}\text{-}A_{control})/(A_{nanoprobe}\text{-}A_{blank}) \times 100\%$.

Atherosclerosis Model Construction and Validation

Model Group

C57BL/6 apolipoprotein E-deficient ($ApoE^{-/-}$) mice (8 weeks old, male, 20–22 g) were randomly divided into three groups. The high-fat group (n=15) was fed a high-fat diet (42.09% fat, 38.72% carbohydrate and 19.19% protein) for 20 weeks. The low-fat group (n=15) was fed with a high-fat diet for 10 weeks and an ordinary diet (10% fat, 75.9% carbohydrate and 14.1% protein) for another 10 weeks. The control group (n=15) was fed an ordinary diet for 20 weeks. All mice were purchased from Beijing Weitonglihua Laboratory Animal Company. Experiments were performed under a project license (no.: WDRM20201103) granted by the Ethical Committee of Renmin Hospital of Wuhan University and in compliance with the Guide for the Care and Use of Laboratory Animals. The weight of the mice was monitored every 5 weeks until 20 weeks.

Blood and Pathological Tests

After 20 weeks, the levels of serum total cholesterol (TC), low-density lipoprotein cholesterol (LDL-C), high-density lipoprotein cholesterol (HDL-C) and triacylglycerol (TG) were detected in 3 mice randomly selected from each of the three groups. The mice were euthanized after blood collection, and the heart was immediately perfused with PBS and fixed with 4% paraformaldehyde. Frozen sections were prepared of the aortic root for oil red O staining, and oil red O staining was also performed throughout the aorta to examine plaque formation. In addition, hematoxylin-eosin (HE) staining was performed on the major mouse organs (heart, liver, spleen, lung and kidney) for follow-up in vivo safety evaluations before photoacoustic/ultrasonic dual-modal imaging.

Distribution of the cRGD Nanomolecular Probes in vivo by Animal Fluorescence Imaging

To explore the dynamic distribution of the cRGD nanomolecular probes in mice, the probes were labeled with the NIR fluorescent dye 1,1′-dioctadecyl-3,3,3′,3′-tetramethylindotricarbocyanine (DiR, Yuanye Biotech, Shanghai, China). Three mice were randomly selected from each group and injected with 200 μL of 8.0 mg/mL molecular probe solution via the tail vein for fluorescence imaging at 1.5 h, 3 h, 6 h, 12 h and 24 h in vivo. The fluorescence intensities with the exposure time of 1.0 s were compared at each time point, and the best fluorescence enrichment was selected for further study.

In order to further clarify the specific distribution of cRGD nanomolecular probes in vivo, fluorescence imaging of isolated organs was continued. After the molecular probes in the above mice were almost completely metabolized, the same dose of molecular probe solution was injected again, euthanasia was performed at the optimal enrichment time, and the heart, liver, spleen, lung, kidney and aorta of the mice were removed for in vitro fluorescence imaging.

The cRGD Nanomolecular Probe Mediates Photoacoustic/Ultrasonic Dual-Modal Imaging of Atherosclerotic Plaques in vivo

The cRGD-GNR-PFP-NPs molecular probe solution (200 μL, 8 mg/mL) was injected into the tail vein, and photoacoustic imaging was performed on the atherosclerotic plaques in the abdominal aorta of the mice by laser excitation at 780 nm at the optimal imaging time point.

After the cRGD-GNR-PFP-NPs had been completely metabolized in the mice, 200 μL of cRGD-GNR-PFP-NPs was injected into the tail vein again. The optimal section of abdominal aortic plaque was obtained by adjusting the animal's ultrasonic probe (frequency 23 MHz). Then, a LIFU irradiator was used to irradiate the plaques (the same parameters as above), and the changes in appearance on ultrasound for the plaques before and after LIFU irradiation were compared.

Pathological Validation of Atherosclerotic Plaque Vulnerability

After the remain 9 mice were euthanized, the abdominal aorta was removed. The expression of integrin αvβ3 in the abdominal aorta plaque was detected by immunofluorescence, and the accumulation of cRGD-GNR-PFP-NPs in the plaque was determined by measuring the fluorescence of DiI. Moreover, HE staining was performed to observe the morphology of the abdominal aortic plaques, Masson staining was performed to evaluate the content of collagen fibers, and immunohistochemistry was used to detect the expression of cluster of differentiation 68 (CD68), CD31 and alpha-smooth muscle actin (α-SMA). The macrophages in atherosclerotic plaque were identified by CD68.[15] CD31 is a marker that represents neovasculogenesis and is prevalent in unstable plaques.[16,17] The α-SMA could represent the vascular smooth muscle cells in the plaque.[15] Plaque vulnerability was comprehensively evaluated by calculating the vulnerability index (vulnerability index = (CD68 + CD31 content)/(smooth muscle cells + collagen fiber content)×100%),[18,19] and the correlation between plaque vulnerability and photoacoustic imaging intensity was analyzed.

In vivo Safety of Photoacoustic/Ultrasonic Dual-Modal Imaging Mediated by the cRGD Nanomolecular Probes

The levels of creatinine (CREA), alanine aminotransferase (ALT) and aspartate aminotransferase (AST) were detected two hours before euthanasia. HE staining was performed on the major organs (heart, liver, spleen, lung and kidney), and the morphological changes in each organ were observed after photoacoustic/ultrasonic dual-modal imaging.

Statistical Analysis

The experimental data were expressed as Mean ± standard deviation (SD). SPSS 26.0 (IBM, Armonk, NY, USA) was used for statistical analysis, Student's *t* test was used for comparison between the two groups, and One-way ANOVA was used for comparison between the three groups. If the variances were homogeneous, the Tukey's test was used; if the variances were heterogeneous, the Dunnetts T3's test was used for comparison between groups. The significance levels of the differences were set to $*p < 0.05$, $**p < 0.01$ and $***p < 0.001$.

Results

The Basic Characteristics of cRGD-GNR-PFP-NPs

The particle sizes of the GNR-PFP-NPs and cRGD-GNR-PFP-NPs were 197.57±3.55 nm and 258.03±6.75 nm, and the potentials were −17.00±1.42 mV and −9.36±0.53 mV, respectively. The polydispersity index (PDI) of each nanoprobe was 0.083±0.008 and 0.161±0.035, respectively. Thus, the two molecular probes were uniformly dispersed. Most cRGD-GNR-PFP-NPs were sphere-like, with smooth surface, nanoscale size, uniform distribution, and partial aggregation by scanning electron microscopy (Figure 1A). The conjugation of cRGD to the GNR-PFP-NPs was observed by confocal laser microscopy. The DiI-labeled GNR-PFP-NPs showed red fluorescence, while FITC-cRGD showed green fluorescence. The red and green fluorescence of the two channels merged to show orange-yellow fluorescence (Figure 1B). The transmittance of cRGD, the GNR-PFP-NPs and the cRGD-GNR-PFP-NPs was detected in the range of 500–4000 cm^{-1}. The infrared absorption spectrum showed that the cRGD-GNR-PFP-NPs had unique absorption peaks at 1662 cm^{-1} and 1542 cm^{-1}, indicating that cRGD was successfully coupled to the GNR-PFP-NPs. In the ultraviolet wavelength range of 350~900 nm,

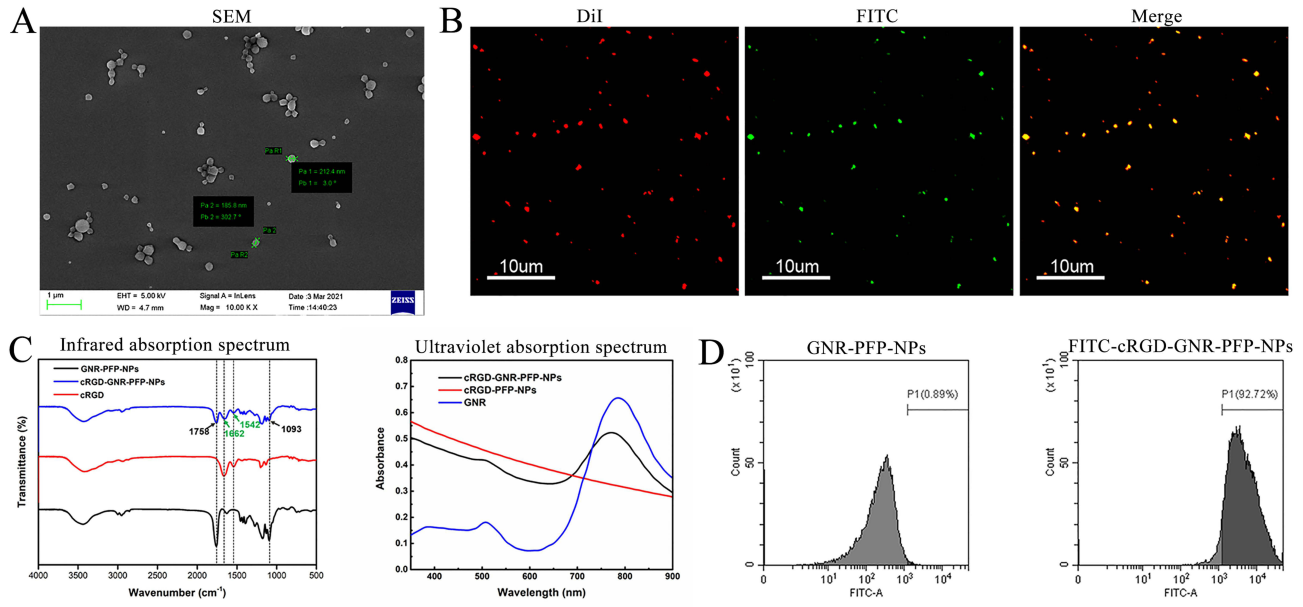

Figure 1 The basic characteristics of the cRGD-GNR-PFP-NPs. (**A**) The appearance feature of cRGD-GNR-PFP-NPs by scanning electron microscopy. Scale bar = 1 μm. (**B**) The DiI-labeled GNR-PFP-NPs showed red fluorescence, while FITC-cRGD displayed green fluorescence. The red and green fluorescence of the two channels merged to show Orange-yellow fluorescence. Scale bar = 10 μm. (**C**) The cRGD-GNR-PFP-NPs infrared and ultraviolet absorption spectrum. (**D**) The conjugation rate of cRGD to GNR-PFP-NPs by flow cytometry.

both cRGD-GNR-PFP-NPs and the GNRs showed characteristic absorption peaks at 780~790 nm, while the cRGD-PFP-NPs without GNRs did not show these analogous peaks (Figure 1C), indicating that the GNRs were successfully loaded. And the successful conjugation rate of cRGD and GNR-PFP-NPs was 92.79%, as determined by flow cytometry (Figure 1D).

The cRGD-GNR-PFP-NPs Phase Transformation/Ultrasonic/Photoacoustic Imaging in vitro

The nanoprobes cRGD-GNR-PFP-NPs could not be observed under the optical microscope without LIFU irradiation in vitro. After 1 min of LIFU irradiation, a small amount of nanoprobes could be observed under the visual field. After 2 min of irradiation, the cRGD-GNR-PFP-NPs could be clearly observed. Both the number and particle size of the nanoprobes increased. 3 min later, the particle size of the cRGD-GNR-PFP-NPs increased significantly and the blasting occurred. The results indicated that the liquid fluorocarbons contained in the cRGD-GNR-PFP-NPs underwent obvious liquid-gas phase transition, and the cRGD-GNR-PFP-NPs undergoing phase transformation showed a decreasing trend with continued irradiation (Figure 2).

After LIFU irradiation for 1 min, 2 min, and 3 min, the signal intensity in two-dimensional B-mode ultrasound and contrast modes was continuously enhanced with the extension of irradiation time, but the signal intensity decreased after 3 min (Figure 3A).

The in vitro photoacoustic imaging results showed that cRGD-GNR-PFP-NPs emitted the strongest red acoustic signal at approximately 790 nm, and the intensity of the signal gradually increased with increasing nanoprobe concentration (Figure 3B).

The Safety of the cRGD-GNR-PFP-NPs in vitro

HUVECs were incubated with 0.5–8.0 mg/mL cRGD-GNR-PFP-NPs for 12 h and 24 h, and in each case, the cell survival rates were 97.0%±3.8% and 96.5%±6.2%, 96.8%±4.1% and 94.0%±8.1%, 94.0%±3.5% and 92.4%±6.2%, 94.8%±3.5% and 94.5%±7.1%, 91.2%±5.1% and 94.6%±11.2%, respectively. At the same nanoprobe concentration, there was no significant difference in the cell survival rate between 12 h and 24 h of incubation. Moreover, at the same incubation time, there were no significant differences in cell viability among the groups with different concentrations of the nanoprobe.

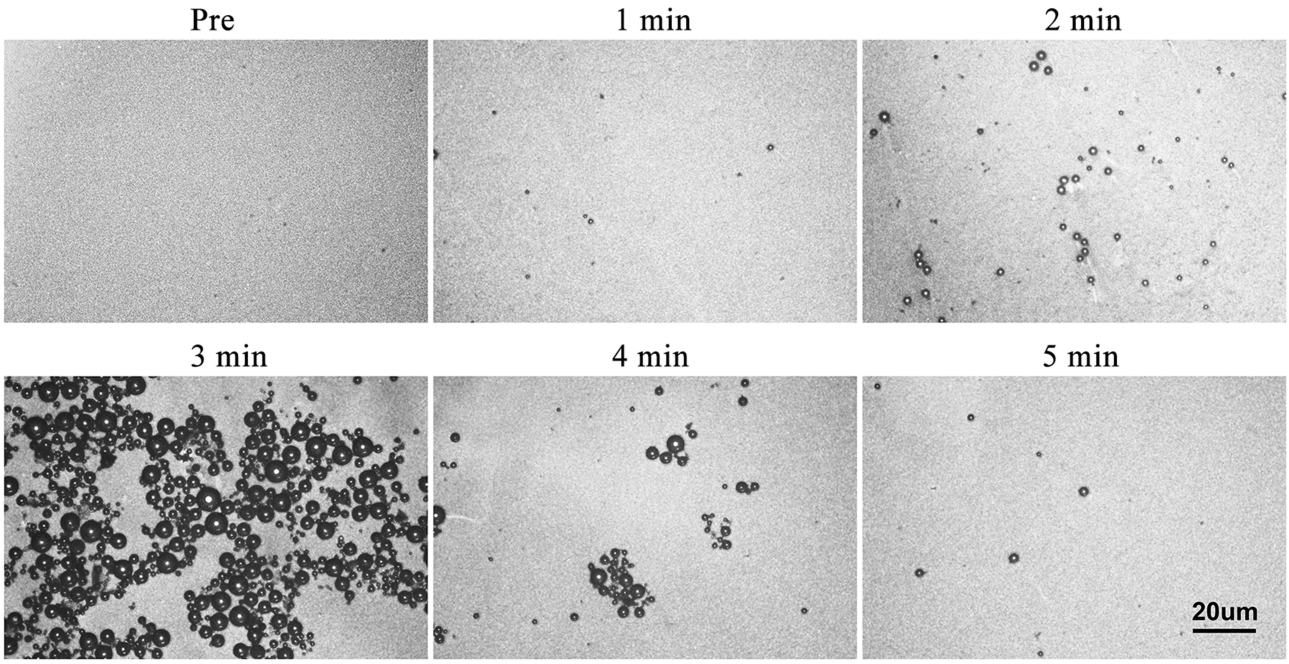

Figure 2 The cRGD-GNR-PFP-NPs phase transformation imaging in vitro. Scale bar = 20 μm.

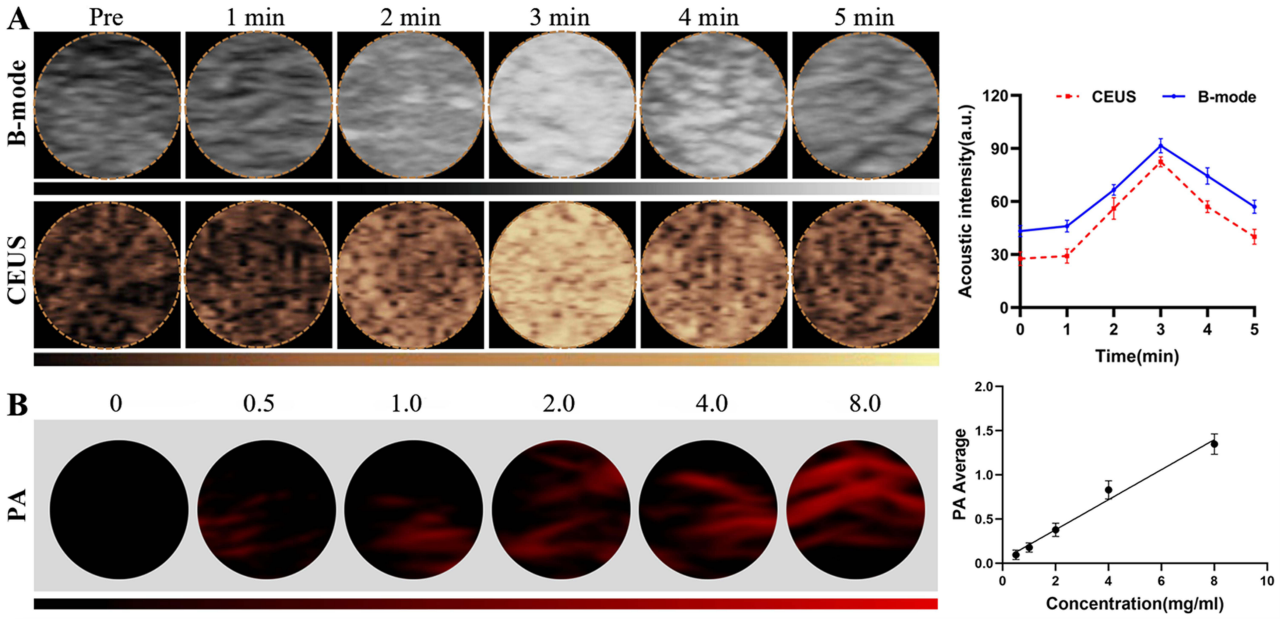

Figure 3 The photoacoustic and ultrasonic imaging of the cRGD-GNR-PFP-NPs. (**A**) The signal intensity changes in two-dimensional B-mode ultrasound and contrast mode. (**B**) The in vitro photoacoustic imaging signal intensity increased with the nanoprobe cRGD-GNR-PFP-NPs concentration.

The Validation of the Atherosclerotic Plaque Model

The body weights of the mice in the three groups showed an increasing trend, and there were no significant differences among the groups at each stage ($P > 0.05$). The Serum TC and LDL-C levels decreased successively in the high-fat group, low-fat group and control group, whereas HDL-C increased successively among the three groups. There was no significant difference in TGs among the three groups with $P > 0.05$ (Figure 4).

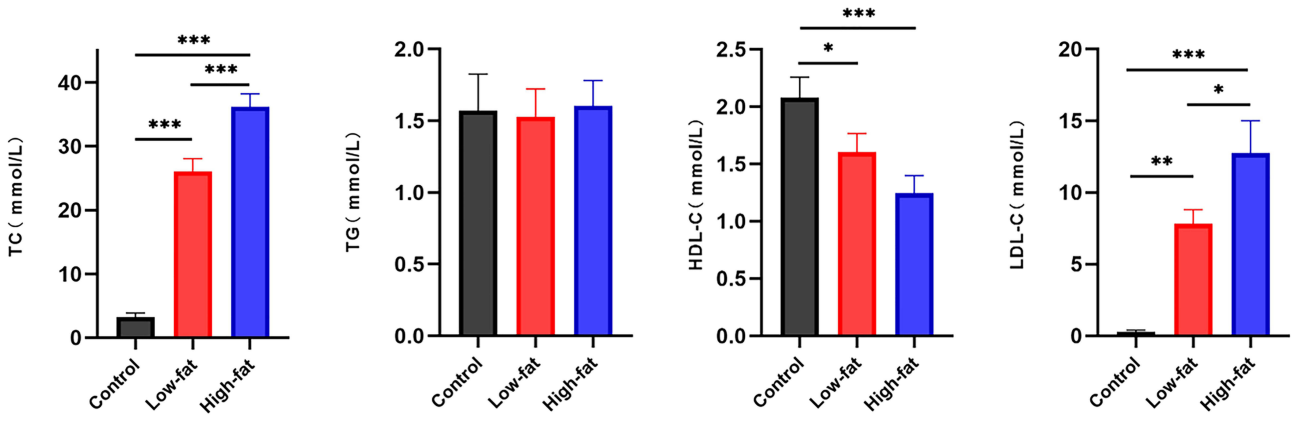

Figure 4 Comparison of serum lipid detection results among three groups of mice (n=3, *p < 0.05, **p < 0.01 and ***p < 0.001).

The oil red O staining images of the aortic root frozen section showed thickened and red-stained areas on the intima of both the low-fat and high-fat groups, while the intima of the control group was smooth and complete with almost no red-stained area. The stained area in the high-fat group (38.38±2.36%) was significantly higher than that in the low-fat group (18.81±2.15%) and the control group (0.83±0.26%) with $P < 0.05$ (Figure 5A).

The oil red O staining images of the whole aorta showed that the atherosclerotic plaque model was successfully constructed with varying degrees of severity. Red-stained lipid plaques were found in the high-fat and low-fat groups and

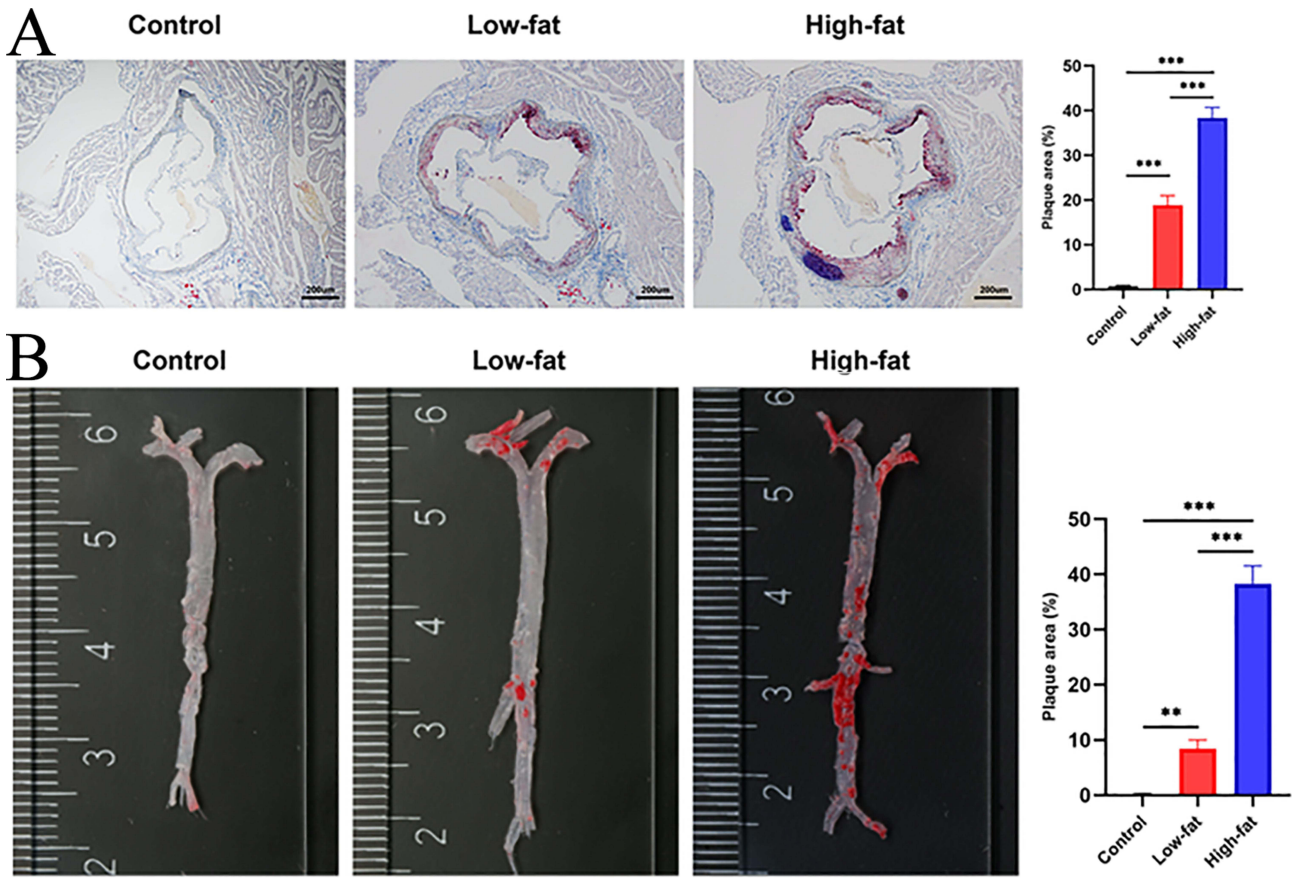

Figure 5 Validation of the atherosclerotic plaque model. (**A**) Frozen section oil red O staining. Scale bar = 200 μm.(n=3, ***p < 0.001). (**B**) The oil red O staining images of the aorta. (n=3, **p < 0.01 and ***p < 0.001).

were concentrated in the bifurcation of the aortic arch and abdominal aorta. The control group showed almost no stained areas. The plaque coverage area in the high-fat group was more extensive, approximately 38.31±3.26%, while those in the low-fat and control groups were 8.45±1.55% and 0.25±0.05%, respectively with $P < 0.05$ (Figure 5B).

The Distribution of the cRGD Nanomolecular Probes in Mice Determined by Animal Fluorescence Imaging

Fluorescence imaging of mice showed that the distribution of the cRGD-GNR-PFP-NPs was approximately uniform in three groups. Moreover, the fluorescence intensity was the strongest at 3 h (1.98×10^8 in the high-fat group, 1.86×10^8 in the low-fat group and 2.06×10^8 in the control group) and then decreased, and a fluorescence signal could not be detected at 24 h. The fluorescence signals near the aortic arch and abdominal aorta were observed at 6 h (1.58×10^8 in the high-fat group, 1.50×10^8 in the low-fat group and 1.46×10^8 in the control group, Figure 6). Therefore, the optimum enrichment time was set to 6 h in this study.

Fluorescence imaging of the isolated organs of the mice 6 h after cRGD-GNR-PFP-NPs infusion showed that there were no significant differences in the distribution of cRGD nanomolecular probes in the lungs, liver, spleen and kidney of the three groups of mice, but there were significant differences in the distribution of the aorta and heart. Compared with the low-fat group and the control group, the aorta and heart of the high-fat group showed the strongest fluorescence signals, which mainly concentrated in the aortic root, arch and branches of the abdominal aorta (Figure 6).

The cRGD Nanomolecular Probes Mediate Photoacoustic/Ultrasonic Imaging of Atherosclerotic Plaques in vivo

Photoacoustic imaging was performed on the abdominal aortas of mice. In both the low-fat group and high-fat group, plaque echo was observed by two-dimensional B-mode ultrasound, while the overall intima in the control group was smooth, and no plaques were observed. In photoacoustic mode, obvious photoacoustic signals were observed on the plaques in the high-fat group, whereas sparse signals were observed in the low-fat group and no signals were observed in the control group (Figure 7A).

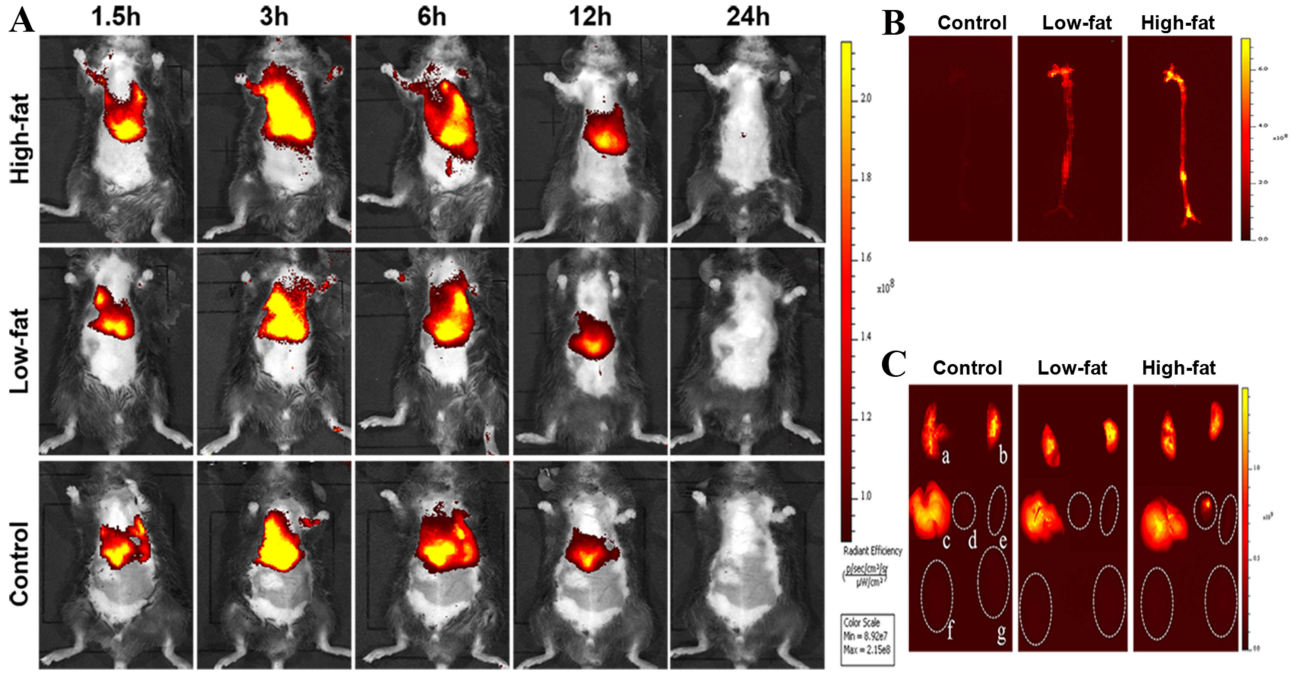

Figure 6 The distribution of the cRGD-GNR-PFP-NPs in mice determined by animal fluorescence imaging. (**A**) Fluorescence imaging of mice in vivo. (**B**) Fluorescence imaging of aorta in vitro. (**C**) Fluorescence imaging of the lung (a and b), liver (c), heart (d), spleen (e) and kidney (f and g) in vitro.

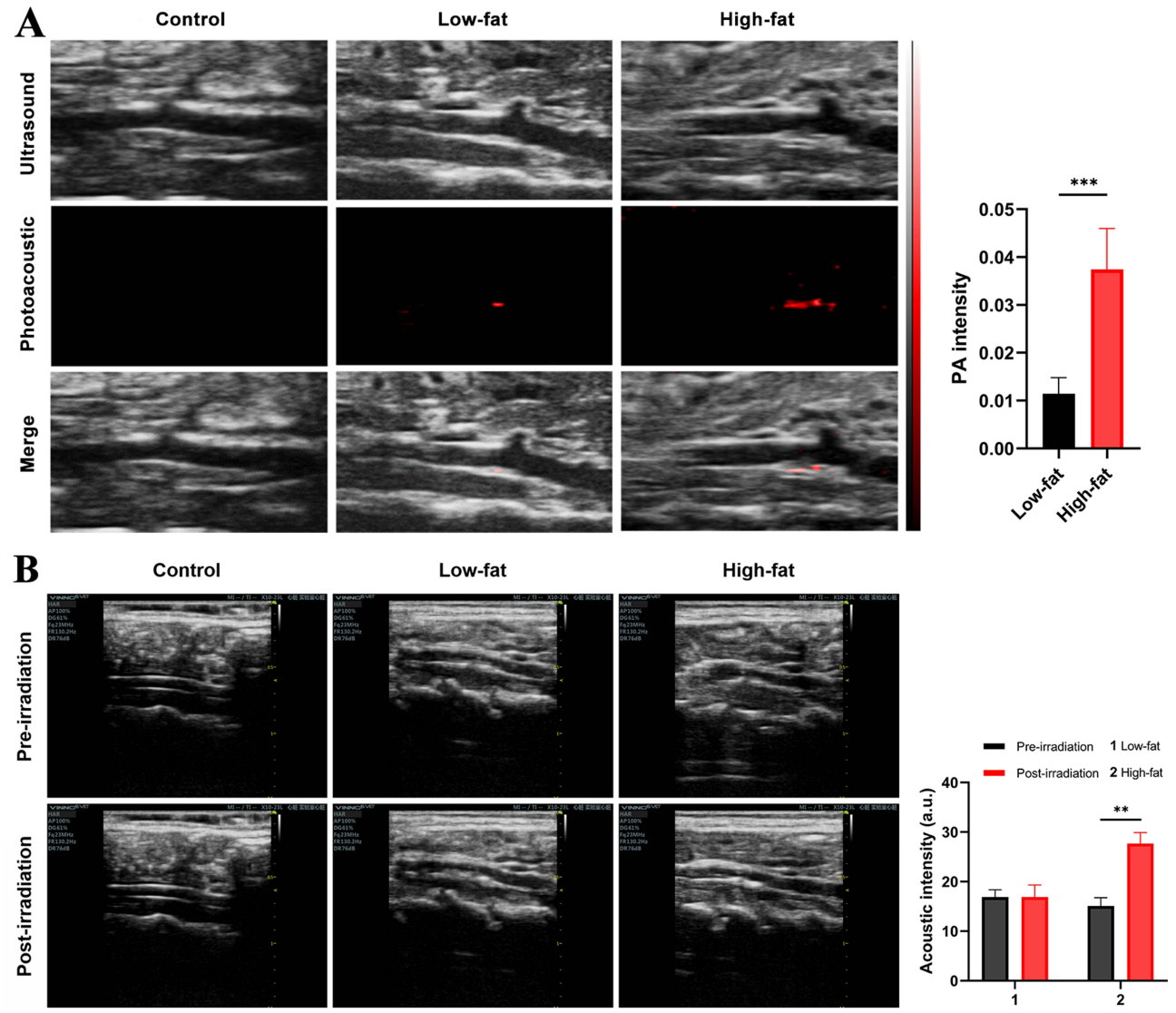

Figure 7 The cRGD nanomolecular probes mediate photoacoustic/ultrasonic imaging of atherosclerotic plaques in vivo. (**A**) the photoacoustic imaging of atherosclerotic plaques. (**B**) the ultrasound imaging of the abdominal aortic plaques before and after LIFU irradiation (n=9, $^{**}p < 0.01$, $^{***}p < 0.001$).

Ultrasound imaging was performed on the abdominal aortic plaques of the mice in the low-fat and high-fat groups. When comparing the changes in plaque echo before and after LIFU irradiation, the plaque and peripheral echo signals were significantly enhanced in the high-fat group, while no significant changes were observed in the low-fat group before and after irradiation (Figure 7B).

Pathological Verification of the Vulnerability of the Atherosclerotic Plaques

The immunofluorescence results showed that the plaques in the high-fat group expressed more integrin αvβ3, which was consistent with cRGD-GNR-PFP-NPs enrichment (Figure 8). HE staining showed that the intima of the arteries in both the low-fat group and the high-fat group was thickened and atherosclerotic plaques convex to the lumen had formed. In contrast, the intima of the arteries in the control group was smooth. The Masson staining images showed that the local plaque collagen fiber content in the high-fat group was lower than that in the low-fat group. The expression of CD68 and CD31 in the high-fat group was also higher than that in the low-fat group, but there was no significant difference in α-SMA expression between the two groups. The vulnerability index of the high-fat group was significantly higher than that of the low-fat group, and the plaque photoacoustic signal intensity was positively correlated with the vulnerability index ($r = 0.93$, $P < 0.05$) (Figure 9).

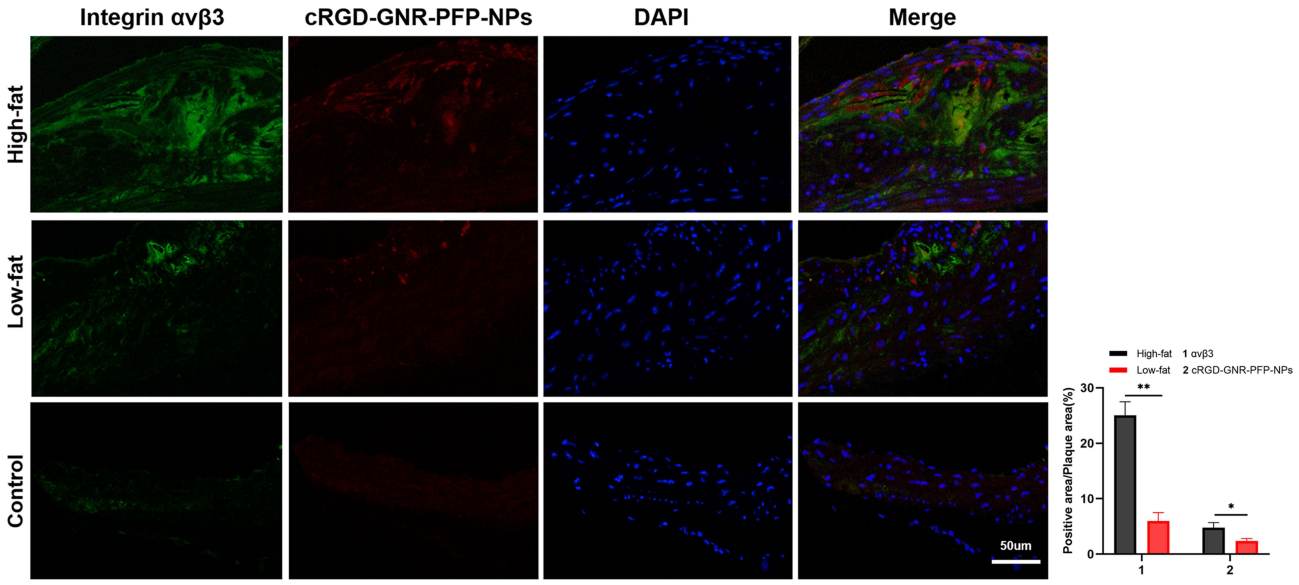

Figure 8 The immunofluorescence results of the plaques expressed integrin αvβ3 and the cRGD-GNR-PFP-NPs enrichment in the three groups. Scale bar = 50 μm. (n=3, *$p < 0.05$ and **$p < 0.01$).

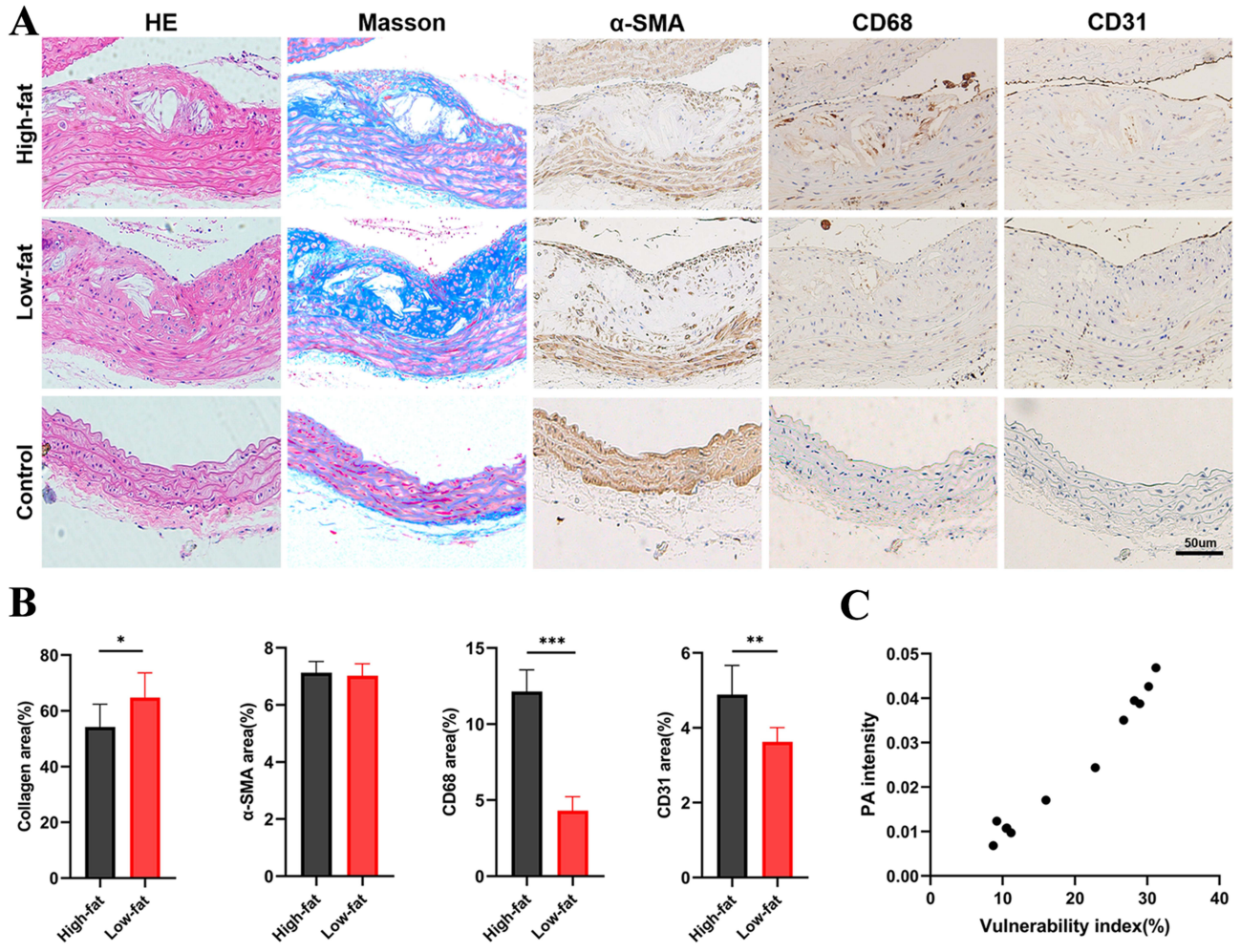

Figure 9 Assessment of the atherosclerotic plaque by pathology. (**A**) The HE, Masson staining and immunohistochemistry were used to detect the atherosclerotic plaque. Scale bar = 50 μm. (**B**) Quantitative analysis of pathological sections (n=6, *$p < 0.05$, **$p < 0.01$ and ***$p < 0.001$). (**C**) The correlation between vulnerability index and the plaque photoacoustic signal intensity ($r = 0.93$, $P < 0.05$).

The Safety of cRGD Nanomolecular Probe-Mediated Photoacoustic/Ultrasonic Dual-Modal Imaging in vivo

There were no significant differences in the serum CREA, ALT and AST levels before and after photoacoustic/ultrasonic dual-modal imaging among the three groups (Figure 10). Additionally, the HE staining results showed no significant changes in the morphology of the major organs (Figure 11), suggesting that using the cRGD-GNR-PFP-NPs for photoacoustic/ultrasonic dual-modal imaging to assess plaque vulnerability showed no significant damage to major organs.

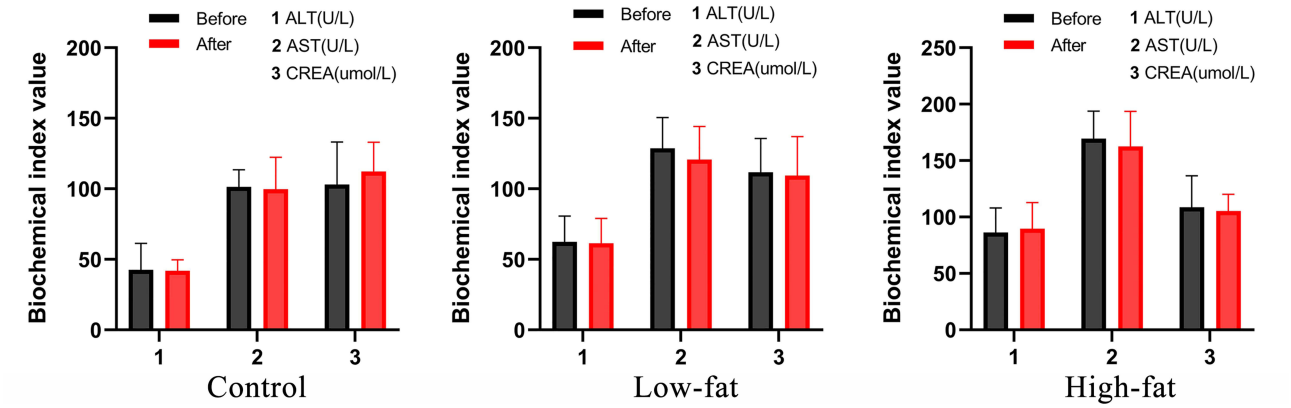

Figure 10 Serum alanine aminotransferase (ALT), aspartate aminotransferase (AST) and creatinine (CREA) levels before and after photoacoustic/ultrasonic dual-modal imaging among the three groups (n=3, all $p > 0.05$).

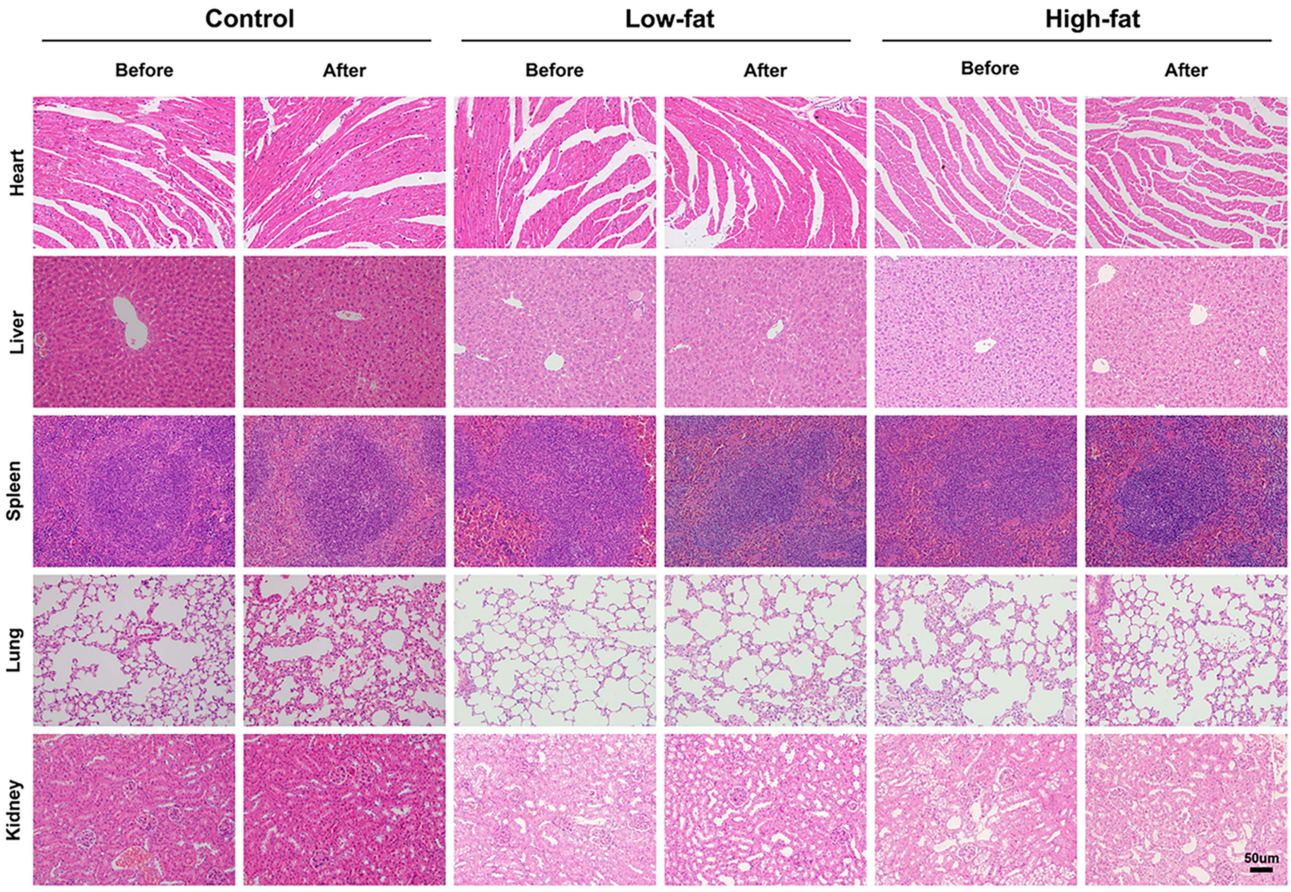

Figure 11 The HE staining results of the major organs (heart, liver, spleen, lung and kidney) before and after cRGD nanomolecular probe-mediated photoacoustic/ultrasonic dual-modal imaging in vivo. Scale bar = 50 μm.

Discussion

Accurate assessment of atherosclerotic plaque vulnerability will help clinicians predict disease risk in a timely manner and determine the best treatment time to greatly reduce the incidence of malignant events caused by sudden plaque rupture. However, the existing imaging technologies cannot accurately monitor plaque vulnerability, so there is an urgent need to develop new methods to achieve this goal. A previous study used molecular imaging of plaque biomarkers to understand the plaque components, which confirmed the feasibility of using this method to monitor the vulnerability of atherosclerotic plaques to a certain extent.[20] However, this method did not allow dynamic monitoring in real time and was somewhat invasive. In this study, on the basis of previous studies, emerging photoacoustic/ultrasonic imaging was used to monitor atherosclerotic plaques. High-quality imaging modalities and convenient imaging methods are expected to allow an accurate assessment in real time and dynamic monitoring of plaque vulnerability with a noninvasive manner.

Photoacoustic imaging was playing an increasingly important role in detecting vulnerable plaques.[21,22] In this study, a novel photoacoustic/ultrasonic dual-modal cRGD nanomolecular probe with a good photoacoustic imaging effect was successfully prepared. GNR was an excellent photoacoustic contrast agent due to its strong absorption peak and high photoacoustic conversion efficiency in the NIR. Therefore, GNR was adopted in this study as one of the cores of nanomolecular probes to achieve the purpose of enhancing photoacoustic imaging.[23] In order to verify the photoacoustic imaging effect of cRGD-GNR-PFP-NPs, experiments had been conducted in vitro and in vivo. The results showed that GNR-loaded nanomolecular probes could generate photoacoustic signals, especially when the NIR excitation wavelength was near 780~790 nm, cRGD-GNR-PFP-NPs could generate obvious photoacoustic signals. It was also found that the photoacoustic signal increased almost linearly with the increase of the concentration of nanomolecular probes. Therefore, the prepared nanomolecular probe could be well used in photoacoustic imaging.

The results of this study showed that the prepared nanomolecular probes can undergo phase transition after LIFU irradiation. The particle size of cRGD-GNR-PFP-NPs increased gradually after irradiation, and with the extension of irradiation time, the particle size further increased and burst, and the number of formed microbubbles gradually decreased. This indicated that liquid fluorocarbon PFP was effectively encapsulated, and liquid-gas phase transition occurred under LIFU irradiation, thus increasing the particle size of cRGD-GNR-PFP-NPs nanoprobes. With the prolongation of irradiation time, a large number of nanobubbles underwent phase transition and rupture. Previous studies had shown that after liquid fluorocarbons were encapsulated into nano-sized particles, the surrounding Laplace pressure increased significantly, and the gasification threshold also increased.[24] In this study, PFP with a relatively low boiling temperature (29 °C) was selected as the core of the nanomolecular probe, and compared with liquid fluorocarbons with a higher boiling point, the threshold of acoustic phase transition of PFP nanoprobes was lower, and thus cavitation effect was more likely to be induced under LIFU irradiation, which provided a guarantee for the subsequent enhancement of ultrasonic development effect. The results of ultrasonic imaging experiments in vitro further showed that the phase transformation of cRGD-GNR-PFP-NPs can significantly enhance the ultrasonic imaging effect, and the development becomes more and more enhanced with the increasing of phase transformation degree, which was related to the acoustic impedance caused by the gas phase microbubbles generated after the phase transformation.

ApoE$^{-/-}$ mice have been widely used in the study of atherosclerotic plaques, as the pathological process of plaque formation in these ideal model animals is similar to that in large animal models.[25] ApoE$^{-/-}$ mice have severely impaired plasma lipoprotein clearance and can develop obvious hypercholesterolemia even in the absence of environmental or mental stimulation due to defects in the apolipoprotein E gene. Moreover, their sensitivity to dietary fat and cholesterol is intensified, leading to more obvious hyperlipidemia.[26] In this study, different feeding patterns were used to build plaque models with different degrees of atherosclerotic vulnerability. The weights of the animals in all groups increased during feeding, and there were no significant differences in body weight among the groups. After 20 weeks of feeding, the TC and LDL-C levels in the high-fat group were significantly higher than those in the low-fat and control groups, while the level of HDL-C was significantly lower in the former group than those in the latter two groups. The results of aortic oil red O staining showed that changes occurred in the atherosclerotic plaques in both the high-fat group and the low-fat group and were concentrated in the bifurcation of the aortic vessels, which was consistent with previous studies.[27] The plaques in the high-fat group were more obvious and covered a wider area. The above lipid profiles and aortic oil red O staining data verified the successful establishment of the atherosclerotic plaque model.

To further understand the metabolic distribution of the cRGD nanomolecular probe in mice and the optimal enrichment time, in vivo fluorescence imaging of mice was performed at different time points after intravenous injection the probes, and the results showed that the localization, distribution and intensity of fluorescence in the mice in the three groups had roughly the same trends over time. The fluorescence signals indicating the approximate location of the aortic arch and abdominal aorta were detected in the high-fat group of mice only at 6 h after probe injection. These data were consistent with the plaque location determined by gross oil red O staining, suggesting that the cRGD nanomolecular probe has a high capability to target atherosclerotic plaques and that its accumulation in the plaque is most obvious 6 h after entering the blood circulation. Therefore, 6 h can be used as the best time point for subsequent photoacoustic/ultrasonic imaging. After 24 h, the fluorescence signal in the three groups of mice disappeared, indicating that the probe can be completely metabolized by the mice by this time.

Photoacoustic/ultrasonic imaging was performed on the atherosclerotic plaques in the abdominal aortas of mice at the optimal time (6 h). Photoacoustic imaging showed that the RGD nanomolecular probe had a good imaging effect in vivo. An obvious photoacoustic signal was observed in the high-fat group, while only a few photoacoustic signals were observed in the low-fat group. The difference in the photoacoustic signals between these groups indicated the greater enrichment of the cRGD-GNR-PFP-NPs in the vulnerable plaques in the high-fat group. The ultrasonic imaging results showed that the cRGD nanomolecular probe combined with LIFU irradiation could enhance the echo intensity of plaques in the high-fat group, but no significant change was observed in the low-fat group. In other words, phase transformation of the probes can be induced by LIFU irradiation to enhance the ultrasonic development effect. Therefore, it is speculated that the difference in ultrasonic development after LIFU irradiation between the high-fat group and the low-fat group is related to the amount of cRGD-GNR-PFP-NPs enriched in the plaque. Furthermore, it is suggested that the RGD nanomolecular probe has a high degree of atherosclerotic plaque targeting.

To confirm that the cRGD nanomolecular probe can be used as a photoacoustic/ultrasonic dual-modal molecular probe that targets integrin αvβ3 expressed in plaques, pathological verification was performed. Immunofluorescence analysis showed that the expression level of integrin αvβ3 in plaques in the high-fat group was significantly higher than that in the low-fat group. Additionally, the enrichment of the cRGD-GNR-PFP-NPs was consistent with the expression of integrin αvβ3 and the probe were colocalized, suggesting that cRGD-GNR-PFP-NPs could specifically target integrin αvβ3 expressed on plaques. Therefore, the cRGD-GNR-PFP-NPs can be used as photoacoustic/ultrasonic dual-modal molecular probes that target integrin αvβ3 in atherosclerotic plaques.

The results of the plaque vulnerability assessment showed that the plaques in the high-fat group were more vulnerable than those in the low-fat group. On the one hand, feeding $ApoE^{-/-}$ mice a high-fat diet for a long time increased both the area and vulnerability of the plaques. On the other hand, it was verified that plaque vulnerability and integrin αvβ3 expression were consistent, and correlation analysis indicated that plaque photoacoustic signal intensity was significantly positively correlated with plaque vulnerability. Therefore, the cRGD nanomolecular probe can not only mediate photoacoustic/ultrasonic dual-modal molecular imaging of atherosclerotic plaques but also effectively assess plaque vulnerability. This was consistent with the results of Liu et al[28] by constructing αvβ3-integrin-targeted ultrasmall gold nanorods with cRGD to evaluate the plaque vulnerability indicators. The immunohistochemical results indicated that αvβ3-integrin was upregulated with increasing aggravation of the lesions. In vivo photoacoustic computed tomography/ultrasonic imaging showed good consistency with αvβ3-integrin expression. Therefore, it indicated that αvβ3-integrin was an effective indicator of plaque instability.

The results of in vitro cell experiments showed that the cRGD-GNR-PFP-NPs had no significant effect on cell survival. LIFU is a relatively safe stimulus, and it has been widely used to induce phase change in nanoprobes to enhance ultrasound imaging and drug release.[29,30] Many studies have used its cavitation effect to treat tumors, plaques and thrombi while demonstrating its good biosafety.[31–33] In vivo study results have showed that there were no significant differences in the serological indexes or pathological morphology of major organs before and after photoacoustic/ultrasonic imaging in atherosclerotic mice, suggesting that cRGD nanomolecular probe-mediated photoacoustic/ultrasonic imaging is a safe method for detecting vulnerable plaques.

Conclusion

In this study, a photoacoustic/ultrasonic dual-modal cRGD nanomolecular probe with good imaging ability was successfully prepared. This cRGD nanomolecular probe can accurately evaluate atherosclerotic plaques vulnerability, verified by histologic studies, significantly increased the information for identifying vulnerable plaques, which can be of great importance in stratifying the risk of cardiovascular and cerebrovascular diseases, especially in asymptomatic patients with good biosafety.

Acknowledgments

This study was supported by the National Natural Science Foundation of China (81901757) and the Natural Science Foundation of Hubei Province (No. 2024AFB883 and No. 2023AFB172).

Author Contributions

All authors made a significant contribution to the work reported, whether that is in the conception, study design, execution, acquisition of data, analysis and interpretation, or in all these areas; took part in drafting, revising or critically reviewing the article; gave final approval of the version to be published; have agreed on the journal to which the article has been submitted; and agree to be accountable for all aspects of the work.

Disclosure

The authors declare that there are no conflicts of interest in this work.

References

1. Papaioannou TG, Kalantzis C, Katsianos E, Sanoudou D, Vavuranakis M, Tousoulis D. Personalized Assessment of the Coronary Atherosclerotic Arteries by Intravascular Ultrasound Imaging: hunting the Vulnerable Plaque. *J Pers Med*. 2019;9(1):8. doi:10.3390/jpm9010008
2. Newman AAC, Cyr Y, Moore KJ. Advancing therapeutic targeting of the vulnerable plaque. *Eur Heart J*. 2022;43(19):1878–1880. doi:10.1093/eurheartj/ehac060
3. Mu D, Wang W, Li J, et al. Ultrasmall Fe (III)-Tannic Acid Nanoparticles To Prevent Progression of Atherosclerotic Plaques. *ACS Appl Mater Interfaces*. 2021;13(29):33915–33925. doi:10.1021/acsami.1c09480
4. Gao B, Xu J, Zhou J, et al. Multifunctional pathology-mapping theranostic nanoplatforms for US/MR imaging and ultrasound therapy of atherosclerosis. *Nanoscale*. 2021;13(18):8623–8638. doi:10.1039/d1nr01096d
5. Li XN, Yin WH, Sun Y, et al. Identification of pathology-confirmed vulnerable atherosclerotic lesions by coronary computed tomography angiography using radiomics analysis. *Eur Radiol*. 2022;32(6):4003–4013. doi:10.1007/s00330-021-08518-0
6. Bouché M, Hsu JC, Dong YC, Kim J, Taing K, Cormode DP. Recent Advances in Molecular Imaging with Gold Nanoparticles. *Bioconjug Chem*. 2020;31(2):303–314. doi:10.1021/acs.bioconjchem.9b00669
7. Li Q, Lin X, Fan Y, et al. Dual-sonosensitizer loaded phase-transition nanoparticles with tumor-targeting for synergistically enhanced sonodynamic therapy. *Biomater Sci*. 2021;9(18):6126–6141. doi:10.1039/d1bm00918d
8. Fales AM, Vogt WC, Wear KA, Ilev IK, Pfefer TJ. Pulsed laser damage of gold nanorods in turbid media and its impact on multi-spectral photoacoustic imaging. *Biomed Opt Express*. 2019;10(4):1919–1934. doi:10.1364/BOE.10.001919
9. Wang X, Mao Y, Sun C, Zhao Q, Gao Y, Wang S. A versatile gas-generator promoting drug release and oxygen replenishment for amplifying photodynamic-chemotherapy synergetic anti-tumor effects. *Biomaterials*. 2021;276:120985. doi:10.1016/j.biomaterials.2021.120985
10. Beer AJ, Pelisek J, Heider P, et al. PET/CT imaging of integrin αvβ3 expression in human carotid atherosclerosis. *JACC Cardiovasc Imaging*. 2014;7(2):178–187. doi:10.1016/j.jcmg.2013.12.003
11. Jiang L, Zhu H, Li Y, Wu X, Wang H, Cheng Z. Detecting Vulnerable Atherosclerotic Plaques by ^{68}Ga-Labeled Divalent Cystine Knot Peptide. *Mol Pharm*. 2019;16(3):1350–1357. doi:10.1021/acs.molpharmaceut.8b01291
12. Pan D, Pramanik M, Senpan A, et al. Molecular photoacoustic imaging of angiogenesis with integrin-targeted gold nanobeacons. *FASEB J*. 2011;25(3):875–882. doi:10.1096/fj.10-171728
13. Lin L, Xie Z, Xu M, et al. IVUS\IVPA hybrid intravascular molecular imaging of angiogenesis in atherosclerotic plaques via RGDfk peptide-targeted nanoprobes. *Photoacoustics*. 2021;22:100262. doi:10.1016/j.pacs.2021.100262
14. Cui C, Yang Z, Hu X, et al. Organic Semiconducting Nanoparticles as Efficient Photoacoustic Agents for Lightening Early Thrombus and Monitoring Thrombolysis in Living Mice. *ACS Nano*. 2017;11(3):3298–3310. doi:10.1021/acsnano.7b00594
15. Goncalves I, Sun J, Tengryd C, et al. Plaque Vulnerability Index Predicts Cardiovascular Events: a Histological Study of an Endarterectomy Cohort. *J Am Heart Assoc*. 2021;10(15):e021038. doi:10.1161/JAHA.120.021038
16. Lavie L, Si-On E, Hoffman A. Markers of Carotid Plaque Destabilization in Patients With Sleep-Disordered Breathing. *Front Neurol*. 2022;13:811916. doi:10.3389/fneur.2022.811916
17. Ignatyev IM, Gafurov MR, Krivosheeva NV. Criteria for carotid atherosclerotic plaque instability. *Ann Vasc Surgery*. 2021;72:340–349. doi:10.1016/j.avsg.2020.08.145
18. Guo S, Zhang S, Chen K, Chen X, Hu F . Effects of diagnostic ultrasound with cRGD-microbubbles on simultaneous detection and treatment of atherosclerotic plaque in ApoE$^{-/-}$ mice. *Front Cardiovasc Med*. 2022;9:946557. doi:10.3389/fcvm.2022.946557

19. Mao Y, Liu XQ, Song Y, et al. Fibroblast growth factor-2/platelet-derived growth factor enhances atherosclerotic plaque stability. *J Cell Mol Med*. 2020;24(1):1128–1140. doi:10.1111/jcmm.14850
20. Wang J, Wu M, Chang J, et al. Scavenger receptor-AI-targeted ultrasmall gold nanoclusters facilitate in vivo MR and ex vivo fluorescence dual-modality visualization of vulnerable atherosclerotic plaques. *Nanomedicine*. 2019;19:81–94. doi:10.1016/j.nano.2019.04.003
21. Schneider MK, Wang J, Kare A, et al. Combined near infrared photoacoustic imaging and ultrasound detects vulnerable atherosclerotic plaque. *Biomaterials*. 2023;302:122314. doi:10.1016/j.biomaterials.2023.122314
22. Muller JW, van Hees R, van Sambeek M, et al. Towards in vivo photoacoustic imaging of vulnerable plaques in the carotid artery. *Biomed Opt Express*. 2021;12(7):4207–4218. doi:10.1364/BOE.430064
23. Salah D, Moghanm FS, Arshad M, et al. Polymer-Peptide Modified Gold Nanorods to Improve Cell Conjugation and Cell labelling for Stem Cells Photoacoustic Imaging. *Diagnostics*. 2021;11(7):1196. doi:10.3390/diagnostics11071196
24. Shin U, Kim J, Lee J, et al. Development of ^{64}Cu-loaded Perfluoropentane Nanodroplet: a Potential Tumor Theragnostic Nano-carrier and Dual-Modality PET-Ultrasound Imaging Agents. *Ultrasound Med Biol*. 2020;46(10):2775–2784. doi:10.1016/j.ultrasmedbio.2020.05.019
25. Jawień J, Nastałek P, Korbut R. Mouse models of experimental atherosclerosis. *J Physiol Pharmacol*. 2004;55(3):503–517.
26. Emini Veseli B, Perrotta P, De Meyer GRA, et al. Animal models of atherosclerosis. *Eur J Pharmacol*. 2017;816:3–13. doi:10.1016/j.ejphar.2017.05.010
27. Nakashima Y, Plump AS, Raines EW, Breslow JL, Ross R. ApoE-deficient mice develop lesions of all phases of atherosclerosis throughout the arterial tree. *Arterioscler Thromb*. 1994;14(1):133–140. doi:10.1161/01.atv.14.1.133
28. Liu X, Gao R, Chen C, et al. Noninvasive photoacoustic computed tomography/ultrasound imaging to identify high-risk atherosclerotic plaques. *Eur J Nucl Med Mol Imaging*. 2022;49(13):4601–4615. doi:10.1007/s00259-022-05911-9
29. Wang M, Yang Q, Li M, et al. Multifunctional Nanoparticles for Multimodal Imaging-Guided Low-Intensity Focused Ultrasound/Immunosynergistic Retinoblastoma Therapy. *ACS Appl Mater Interfaces*. 2020;12(5):5642–5657. doi:10.1021/acsami.9b22072
30. Qin H, Teng R, Liu Y, Li J, Yu M. Drug Release from Gelsolin-Targeted Phase-Transition Nanoparticles Triggered by Low-Intensity Focused Ultrasound. *Int J Nanomed*. 2022;17:61–71. doi:10.2147/IJN.S341421
31. Ye M, Zhou J, Zhong Y, et al. SR-A-Targeted Phase-Transition Nanoparticles for the Detection and Treatment of Atherosclerotic Vulnerable Plaques. *ACS Appl Mater Interfaces*. 2019;11(10):9702–9715. doi:10.1021/acsami.8b18190
32. Yang A, Qiao B, Strohm EM, et al. Thrombin-responsive engineered nanoexcavator with full-thickness infiltration capability for pharmaceutical-free deep venous thrombosis theranostics. *Biomater Sci*. 2020;8(16):4545–4558. doi:10.1039/d0bm00917b
33. Zhou J, Hou J, Liu S, et al. Theranostic Nanoplatform with Sequential SDT and ADV Effects in Response to Well-Programmed LIFU Irradiation for Cervical Cancer. *Int J Nanomed*. 2021;16:7995–8012. doi:10.2147/IJN.S339257